VIP Supramolecular Chemistry Very Important Paper

How to cite: *Angew. Chem. Int. Ed.* **2023**, *62*, e202211776
International Edition: doi.org/10.1002/anie.202211776
German Edition: doi.org/10.1002/ange.202211776

Confinement-Driven Photophysics in Hydrazone-Based Hierarchical Materials

Grace C. Thaggard, Gabrielle A. Leith, Daniil Sosnin, Corey R. Martin, Kyoung Chul Park, Margaret K. McBride, Jaewoong Lim, Brandon J. Yarbrough, Buddhima K. P. Maldeni Kankanamalage, Gina R. Wilson, Austin R. Hill, Mark D. Smith, Sophya Garashchuk, Andrew B. Greytak, Ivan Aprahamian, and Natalia B. Shustova**

Abstract: Confinement-imposed photophysics was probed for novel stimuli-responsive hydrazone-based compounds demonstrating a conceptual difference in their behavior within 2D versus 3D porous matrices for the first time. The challenges associated with photoswitch isomerization arising from host interactions with photochromic compounds in 2D scaffolds could be overcome in 3D materials. Solution-like photoisomerization rate constants were realized for sterically demanding hydrazone derivatives in the solid state through their coordinative immobilization in 3D scaffolds. According to steady-state and time-resolved photophysical measurements and theoretical modeling, this approach provides access to hydrazone-based materials with fast photoisomerization kinetics in the solid state. Fast isomerization of integrated hydrazone derivatives allows for probing and tailoring resonance energy transfer (ET) processes as a function of excitation wavelength, providing a novel pathway for ET modulation.

Introduction

Progress in materials with dynamically-controlled properties, which are demanded by industry-driven applications and therefore, next-generation advancements in the technology and energy sectors, are directly correlated with stimuli-responsive building block development.[1–22] Advances in this field are mainly associated with several well-known families of photochromic molecules, e.g., azobenzene, diarylethene, spiropyran, or viologen derivatives.[23–38] At the same time, hydrazone-based compounds experienced a renaissance in 2009 and, thus far, have attracted a significant interest because of their bistable behavior with tailorable half-lives ranging from minutes to thousands of years, large photostationary state (PSS) ratios, and relatively high photoisomerization quantum yields.[39–41] Despite the listed advantages, industry-driven applications, and a number of remarkable solution-based studies, the development of hydrazone-based solid-state materials is still in its infancy.[42–47] For example, photoisomerization of hydrazone derivatives, which is associated with large structural rearrangements accompanying transitions between two photoisomers, could be impeded in the solid state (Scheme 1).[48–50] The reason for this

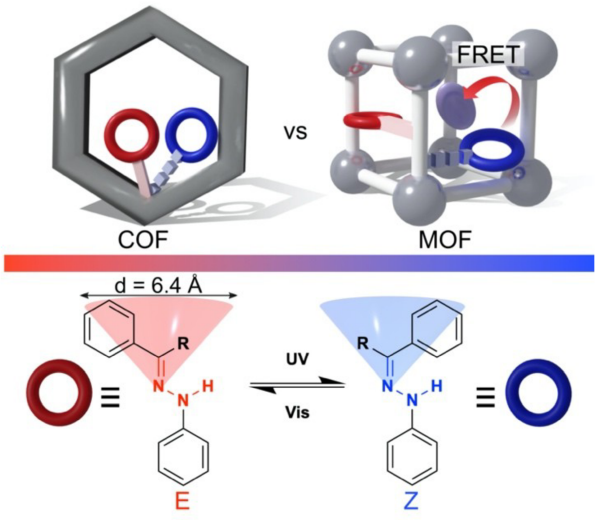

Scheme 1. (*top*) Coordinatively-immobilized hydrazone-based photoswitches within 2D (COF) and 3D (MOF) porous scaffolds, resulting in the ability to tune Förster resonance energy transfer (FRET) processes through excitation wavelength alternation. (*bottom*) Photoisomerization of a hydrazone derivative, and the volume necessary for its photoisomerization is approximated as a cone (red or blue) with a diameter of ca. 6.4 Å.

[*] G. C. Thaggard, Dr. G. A. Leith, K. C. Park, M. K. McBride, Dr. J. Lim, B. J. Yarbrough, B. K. P. Maldeni Kankanamalage, G. R. Wilson, A. R. Hill, Dr. M. D. Smith, Prof. Dr. S. Garashchuk, Prof. Dr. A. B. Greytak, Prof. Dr. N. B. Shustova
Department of Chemistry and Biochemistry, University of South Carolina
Columbia, SC 29208 (USA)
E-mail: shustova@sc.edu

D. Sosnin, Prof. Dr. I. Aprahamian
Department of Chemistry, Dartmouth College
Hanover, NH 03755 (USA)
E-mail: ivan.aprahamian@dartmouth.edu

Dr. C. R. Martin
Savannah River National Laboratory
Aiken, SC 29808 (USA)

behavior is that the hydrazones undergo isomerization involving rotation around the C=N bond in the excited state, allowing for a large volume change (≈ 70 Å^3) that can be roughly approximated as a cone with a rotation radius of ≈ 3.2 Å (Scheme 1).[51–54] For instance, recent studies using thin films have shown that the solid-state behavior of hydrazone derivatives is largely dependent on the presence of voids.[25,46] In particular, hydrazone-based compounds with a high degree of planarity generally exhibit highly ordered packing motifs, which reduces the space available for isomerization.[25,46] In contrast, derivatives in which the phenyl groups rotate out of plane tend to switch in the solid state more efficiently because of amorphous, "loose packing," which affords the space required for photoisomerization to occur.[25,46] Thus, we hypothesize that void preorganization could promote hydrazone isomerization and advance efficient switching in the solid state.[55,56] Well-defined porous materials such as metal-organic and covalent-organic frameworks (MOFs and COFs)[57–77] offer such space for isomerization to occur, and therefore, can be used to promote photochromic performance of hydrazone derivatives. Indeed, herein we demonstrated the realization of this concept for the first time using hydrazone derivatives with light-induced switching which are coordinatively-immobilized within porous MOF and COF scaffolds. Moreover, we revealed the conceptual difference in the photophysical behavior of the hydrazone-based compounds covalently integrated into two-dimensional (2D) versus three-dimensional (3D) scaffolds supported by theoretical modeling. Furthermore, we showed that restricted photoisomerization observed in 2D frameworks could be overcome in 3D matrices, and more importantly, leads to photoisomerization rates very similar to those observed in solution. Comprehensive analysis of the photoresponsive building blocks and corresponding materials include powder and single crystal X-ray diffraction[101] (PXRD and SC-XRD, respectively), time-resolved and steady-state photoluminescence spectroscopy, mass-spectrometry (MS), thermogravimetric analysis (TGA), ^{1}H nuclear magnetic resonance (NMR), ^{13}C cross-polarization magic angle spinning (CP-MAS) NMR, UV/Vis, diffuse reflectance, and Fourier transform infrared (FTIR) spectroscopies, as well as theoretical modeling. Finally, for the first time we probed modulation of energy transfer processes using the ability of hydrazone derivatives to photoisomerize within a porous scaffold.

Results and Discussion

As a first step of our studies, three novel azide-containing hydrazone derivatives have been prepared (Figure 1), ethyl 2-(4-azidophenyl)-2-(2-phenylhydrazineylidene)acetate (**H-1**), ethyl 2-(2-(3-azidophenyl)hydrazineylidene)-2-phenylacetate (**H-2**), ethyl 2-(2-(4-azidophenyl)hydrazineylidene)-2-phenylacetate (**H-3**), and one carboxylate-based derivative, 4-(2-(4-carboxybenzylidene)hydrazineyl)benzoic acid (**H-4**). All derivatives contain reactive groups (i.e., $-N_3$ or –COOH) that allow for integration within the porous scaffolds (see below). Notably, we designed **H-4** without the

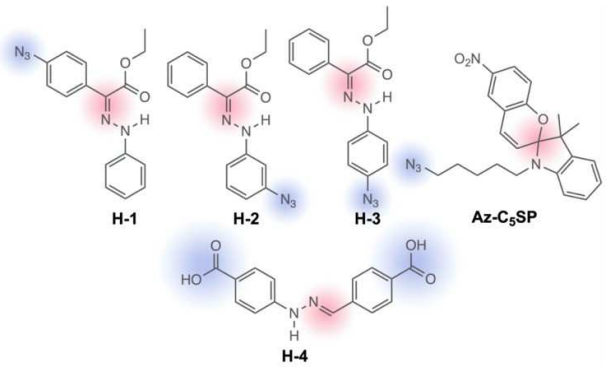

Figure 1. Hydrazone derivatives, **H-1**–**H-4** and a spiropyran-based molecule, **Az-C$_5$SP**, with the reactive functional groups necessary for their integration (highlighted in blue) within a COF or MOF matrix. Photoactive centers are highlighted in pink.

acetyl groups to eliminate potential interference between linker binding to the metal node and the photoactive hydrazone core. The detailed synthetic procedures for their preparation and characterization methods are provided in Supporting Information (Schemes S1 and S2 and Figures S2–S9). After linker preparation, we coordinatively integrated the hydrazone derivatives, **H-1**–**H-3** and **H-4** within the porous COF and MOF scaffolds, respectively. The choice of frameworks was dictated by several criteria. First, the pore size of the selected scaffolds should be sufficient to accommodate bulky photochromic molecules. Second, the framework should provide the mechanisms for post-synthetic installation of the hydrazone linkers (e.g., functional groups, "missing" linkers, or unsaturated metal nodes).[78–87] Finally, the host should maintain structural integrity after coordinative immobilization of hydrazone derivatives and for the duration of the corresponding photophysical experiments. As a result, one COF and two MOFs have been selected as suitable candidates to perform such studies. For instance, the COF (**1**, Schemes 1 and S6) possesses a 30 Å-pore size, consists of organic linkers decorated with reactive alkyne functionalities, and preserves crystallinity over a wide pH range.[67,88,89] Similarly, the Zr-MOF, $Zr_6O_4(OH)_4$-$(BPDC)_6$ (UiO-67; $BPDC^{2-}$ = 4,4′-biphenyldicarboxylate; UiO = University of Oslo), maintains structural integrity in a variety of organic solvents.[90] At the same time, the UiO-67 structure possesses "defects", (i.e., missing linkers, Figure 2) which can be used for installation of hydrazone linkers. In contrast to UiO-67, the second selected Zr-based MOF, $Zr_6O_4(OH)_8(Me_2BPDC)_4$ (PCN-700; H_2Me_2BPDC = 2,2′-dimethyl-4,4′-biphenyldicarboxylic acid; PCN = porous coordination network) contains specific pockets as shown in Figure 2, which could be used for postsynthetic installation of photochromic molecules. Notably, all three mechanisms for hydrazone installation are based on covalent-bond formation, and therefore, prevent photochromic molecule leaching.

Integration of **H-1**, **H-2**, and **H-3** within the COF **1** was carried out using a copper catalyzed azide-alkyne 1,3-cycloaddition (CuAAC) reaction between alkyne functional

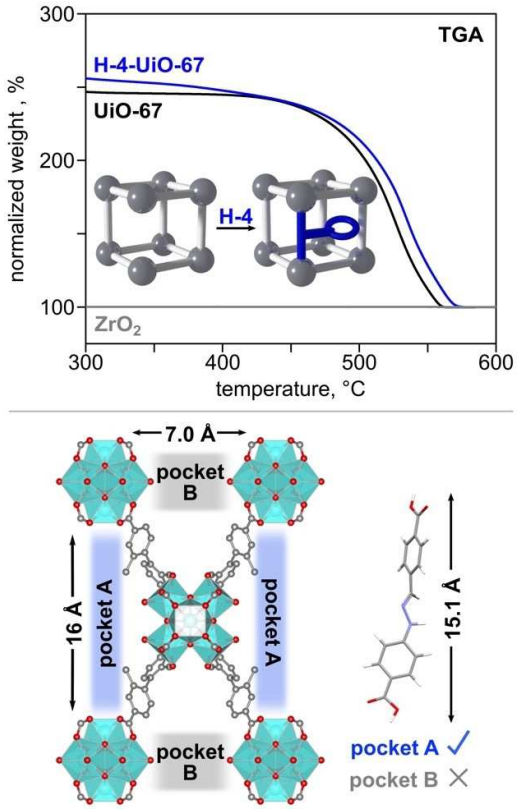

Figure 2. (*top*) TGA plot of ZrO_2 (gray), UiO-67 (black), and **H-4**-UiO-67 (blue). All TGA data was normalized to 100% to a value for ZrO_2 at 600 °C. (*bottom*) Schematic representation of the "A" pockets in PCN-700 available for **H-4** installation. The aqua, red, and gray spheres represent zirconium, oxygen, and carbon atoms, respectively.

groups in the pores and an azide-functionalized hydrazone derivative (Scheme 2, Figures S13–S15 and S19–S21). As a first step, we prepared the two-dimensional COF, **1≡(χ%)** (where $\chi = [BPTA]/([BPTA]+[DMTA]) \times 100\,\%$) using the acid-catalyzed condensation of 2,5-bis(2-propynyloxy) terepthalaldehyde (BPTA), 2,5-dimethoxy terepthalaldehyde (DMTA), and tri-(4-aminophenyl)benzene (TAPB). Varying the ratio of BPTA to DMTA (i.e., changing the value of χ) allows for stoichiometric control of the theoretical maximum amount of installed hydrazone by changing the average number of alkyne functionalities (BPTA) per pore.

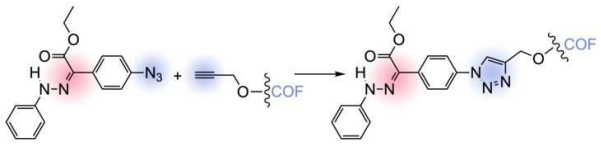

Scheme 2. Representation of azide-functionalized photoswitch integration within the COF scaffold on the example of **H-1**. Reactive functional groups before and after reaction completion are highlighted in blue, and photoactive centers are highlighted in pink.

With this in mind, we prepared a range of alkyne-containing COFs from **1≡(17%)** to **1≡(34%)** to optimize the amount of hydrazone compounds present in the material without inducing steric hindrance for isomerization. The crystallinity of the parent COF after photoswitch installation was confirmed by PXRD analysis (Figures S30–S32), and the presence of alkyne functionalities was monitored through FTIR spectroscopy (Figures S23–S25).

Prior to incorporation of hydrazone derivatives within the extended structure of the COF and to study the photophysical properties of triazole-functionalized hydrazones, we optimized the synthetic conditions using molecular building blocks such as azide-derived hydrazones and benzyl propargyl ether (Scheme S3). For that, the azide-functionalized hydrazones and benzyl propargyl ether were heated in the presence of cupric sulfate and sodium ascorbate at 70 °C overnight, yielding ethyl 2-(4-(4-(phenoxymethyl)-1*H*-1,2,3-triazol-1-yl)phenyl)-2-(2-phenylhydrazineylidene)acetate (**H-5**), ethyl 2-(2-(3-(4-(phenoxymethyl)-1*H*-1,2,3-triazol-1-yl)phenyl)hydrazineylidene)-2-phenylacetate (**H-6**), and ethyl 2-(2-(4-(4-(phenoxymethyl)-1*H*-1,2,3-triazol-1-yl)phenyl)hydrazineylidene)-2-phenylacetate (**H-7**) shown in Scheme S3. A more detailed description of the used synthetic procedure including methods of characterization can be found in the Supporting Information.

Similar synthetic conditions, which were developed for the CuAAC reaction using molecular building blocks, were applied for integration of the azide-functionalized hydrazone derivatives in **1≡(34%)** using a stepwise procedure. First, **1≡(34%)** was exposed to a hydrazone derivative (**H-1**–**H-3**) in a mixture of acetonitrile and water for three days, which promoted diffusion of the reactants into the pores. Only after three-days of pre-soaking, copper(I) iodide and Hünig's base were added to the COF/hydrazone suspension, and the resulting reaction mixture was heated at 55 °C for three days (see the Supporting Information for more details). FTIR spectroscopy was implemented to assess reaction progress in the solid-state by monitoring the stretches centered at 2120 cm^{-1} (C≡C) and 3300 cm^{-1} (H–C≡C). As expected, these stretches were absent in the spectrum of hydrazone-integrated **1≡(34%)** because of the coordinative immobilization of the hydrazone linkers. At the same time, the FTIR spectra of the control experiments, carried out using the same parent COF subjected to the synthetic conditions in the absence of azide-containing molecules, still contain 2120 cm^{-1} and 3300 cm^{-1} stretches (Figures S23–S25). Thus, the disappearance of these bands can be attributed to the coordinative immobilization of the hydrazone linkers within the COF. In addition, we performed NMR spectroscopic analysis of the digested hydrazone-integrated COF samples which clearly indicated the presence of hydrazone derivatives inside the COF matrix (Figures S13–S15). Moreover, we analyzed the product in the solid state by CP-MAS NMR spectroscopy which confirmed the disappearance of C≡C resonances in contrast to the control experiment carried out without the azide precursor (Figures S19–S21). Maintenance of COF structur-

al integrity was confirmed by PXRD analysis before and after hydrazone derivative integration (Figures S30–S32).

In addition to targeting purely-organic COFs, we integrated hydrazone linkers within a 3D MOF matrix. To do this, we synthesized UiO-67 and PCN-700 MOFs as precursors using modified literature procedures,[91,92] and the prepared frameworks were characterized by PXRD, TGA, and FTIR spectroscopy (Figures S27–S29, S34, and S35). These MOFs were chosen due to the possibility of post-synthetic hydrazone derivative installation, appropriate pore sizes, and Zr-metal nodes (Zr^{4+}, d^0) to prevent fluorescence quenching. Coordinative immobilization of **H-4** in both UiO-67 and PCN-700 MOFs was achieved by exposing each MOF to a 30 mM solution of **H-4** at 75 °C for 24 hours (see the Supporting Information for more details). As mentioned before, **H-4** installation occurs in the "A" pockets (16 Å) of PCN-700, which are suitable for **H-4** linker integration (≈15.1 Å, Figure 2), while in the case of UiO-67, the hydrazone-based linker was installed in the place of missing linkers ("defects") as shown in Figure 2. We used NMR spectroscopic studies to confirm integration of **H-4** within each MOF. After an extensive washing procedure using a Soxhlet apparatus and follow up digestion (destroyed in the presence of acid) of the samples, analysis of the ^{1}H NMR spectra showed both MOFs contain hydrazone-based linkers. For instance, in the case of PCN-700, 19 % hydrazone-linker installation (i.e., 1.8 linkers per metal node) was determined based on the NMR spectroscopic analysis (Figure S18). To further evaluate the degree of installation at the defect sites of UiO-67, we performed thermogravimetric analysis of the parent framework to estimate the number of defects per metal node before **H-4** installation. For that, we normalized the weight loss for UiO-67 to 100 % at 600 °C with ZrO_2 serving as a reference.[93] The observed plateau from 300–400 °C was used to estimate the number of linkers present at the metal node (Figure S29). This procedure was repeated after **H-4** installation, and the increase in the number of linkers per node was attributed to coordinated **H-4** photoswitches. As a result, we estimated that 9.7 linkers per node were present in the parent UiO-67 and 10.2 linkers per node in **H-4**-UiO-67. Thus, on average 0.5 hydrazone-based linkers were installed per node (Figures 2 and S17). Maintenance of MOF structural integrity before and after linker installation was confirmed by PXRD analysis (Figures S34 and S35).

After completion of material characterization, we performed photophysical studies on the molecular compounds, **H-4**–**H-7**, and photoswitch-integrated COFs and MOFs. Specifically, we monitored photoisomerization of **H-5**–**H-7** in solution (2×10^{-5} M in toluene) using the ^{1}H NMR resonances centered at 7.9 and 12.7 ppm, which correspond to the amine proton of the *E* and *Z* isomers, respectively (Figures S37–S42). As a result, we observed a decrease of signal at 12.7 ppm and a concurrent increase in the resonance at 7.9 ppm upon irradiation with 410-nm light until a PSS was achieved, which corresponds to isomerization from *Z* to *E* isomers (Figures S38, S40, and S42). Reversion to the initial *Z*/*E* ratio was observed upon excitation with 340-nm irradiation (Figures S38, S40, and S42). As a next step, we monitored the change in absorbance profiles for **H-5** as a function of irradiation using solution UV/Vis spectroscopy. Upon alternation of the wavelength from 410 to 340 nm, a ≈40 nm hypsochromic shift was detected indicating *E*-to-*Z* photoisomerization (Figures S37, S39, and S41). Using a first-order kinetic model, we estimated the photoisomerization rates to be 1.4×10^{-1} s^{-1} ($R^2=0.999$), 5.9×10^{-2} s^{-1} ($R^2=0.997$), and 1.5×10^{-1} s^{-1} ($R^2=0.999$) for *E*-to-*Z* isomerization of **H-5**, **H-6**, and **H-7**, respectively. A summary of these photophysical results can be found in Table S4.

Photoisomerization of **H-1**–**H-3** integrated within the COF was studied by diffuse reflectance (DR) spectroscopy. Specifically, we collected the DR profile of each hydrazone-integrated COF, (e.g., **H-1[1≡(34 %)]**) when stored in the dark and after 5-second-interval exposure to 405-nm light (Figure 3). As expected, we observed an enhancement with extended exposure at 405 nm until a PSS was reached. As a control experiment, we carried out the same studies using the parent COF (i.e., without photoswitch integration), and no changes in the DR spectrum were detected (Figure S53). Similar to photophysical studies performed in solution, we altered the excitation wavelength from 405 to 340 nm with the anticipation of reversible photoswitch behavior, i.e., *E*-to-*Z* photoisomerization (Figure 3). However, irradiation with 340-nm light even for extended periods of time did not result in recovery of the initial pre-treatment DR profile. Analysis of multiple batches of the same material confirmed irreversible photoswitching behavior. Similar photophysical behavior was detected for **H-2[1≡(34 %)]** and **H-3[1≡(34 %)]** (Figures S54 and S55). To shed light on these observations, we attempted to model the geometrical parameters associated with photoisomerization that could impede reversible photoswitching. For that, we considered several low-energy conformers of the photoswitchable moiety (Figures 4 and S1) for which geometry was optimized within a frozen COF pore formed by three 2D layers based on the experimentally confirmed COF structure (Figure S1). Figure 4 demonstrates one of the representative low-energy structures in which the phenyl ring is oriented toward the

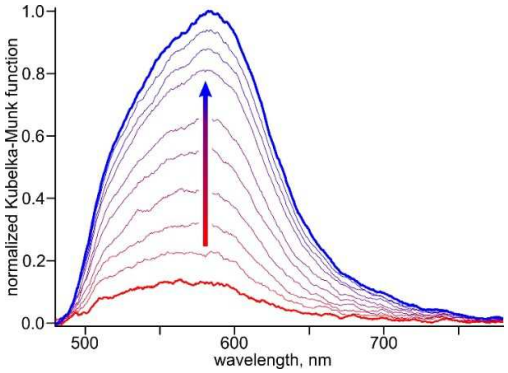

Figure 3. Time-resolved diffuse reflectance spectra demonstrating isomerization from *Z*-**H-1[1≡(34 %)]** (red) into *E*-**H-1[1≡(34 %)]** (blue) upon excitation with 405-nm wavelength.

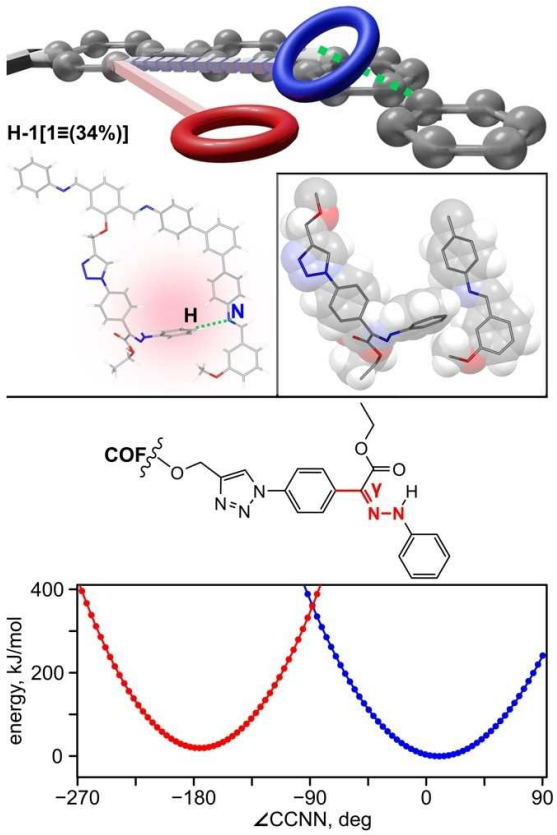

Figure 4. (*top*) Representation of interactions between **H-1** and **1≡(34%)** that could limit photoisomerization of the studied hydrazone-integrated COFs. (*bottom*) Potential energy surface for isomerization of *Z*-**H-1[1≡(34%)]** (red) and *E*-**H-1[1≡(34%)]** (blue).

nitrogen atom of the COF linker with the shortest H···N distance of 2.7 Å. A scan of the dihedral angles, ∠CCNN (γ; *bottom*, Figure 4), shows that the phenyl ring is constrained by the COF within the −15–10° range and requires high-energy rearrangement to escape the original conformation toward the *Z*-isomer. An analogous dihedral angle scan for an *E*-isomer also shows high-energy rearrangement barrier for *E*-to-*Z* isomerization. Considering the spatial extent and conformational flexibility of the photoswitch, the additional possibility is that the large amplitude motion associated with hydrazone isomerization is impeded by the same photochromic molecules in the above and below COF layers. In both scenarios, the motion of the dangling photoswitch fragment is restricted through close interactions between framework and photoswitch moiety (Figures 4 and S1).

For comparison, we also used an azide-functionalized derivative of a more common class of spiropyran photochromic compounds for which isomerization is also accompanied by large structural transformations as in the case of hydrazone derivatives, but the former successfully photoisomerizes when coordinatively immobilized within the porous matrix of MOFs.[94] In particular, we prepared, 1′-(5-azidopentyl)-3′,3′-dimethyl-6-nitrospiro[chromene-2,2′-indoline] (**Az-C$_5$SP**), using a modified literature procedure.[95] Prior to integration inside the COF, we studied its photophysical properties in solution using UV/Vis spectroscopy and epifluorescence microscopy. In particular, we monitored the intensity enhancement in the absorbance profile upon exposure to 365-nm light followed by attenuation under visible light (Figures S56–S58). In addition, we observed an enhancement in emission intensity under UV (λ_{ex} = 330–385 nm) excitation followed by attenuation under visible light. For its integration inside **1≡(17%)**, we employed a similar synthetic procedure as described above. First, **1≡(17%)** was exposed to **Az-C$_5$SP** in a mixture of tetrahydrofuran and water for three days, which promoted diffusion of the reactants into the pores. After three-days of pre-soaking, copper(I) iodide and Hünig's base were added to the COF/**Az-C$_5$SP** suspension, and the resulting reaction mixture was heated at 55 °C for three days (see the Supporting Information for more details). FTIR spectroscopy was used to monitor the reaction progress through disappearance of the stretches centered at 2120 cm^{-1} (C≡C) and 3300 cm^{-1} (H–C≡C, Figure S26, vide supra). Indeed, these resonances were not observed in spectrum of spiropyran-integrated **C$_5$SP[1≡(17%)]**. In addition, ^{1}H NMR spectroscopy of digested **C$_5$SP[1≡(17%)]** and ^{13}C CP-MAS NMR spectroscopy of the solid-state sample also confirmed successful integration of **Az-C$_5$SP** into the COF scaffold (Figures S16 and S22). As in the case of coordinatively immobilized hydrazone derivatives, photophysical studies demonstrated that the integrated spiropyran-based compound also exhibits limited reversibility, which supports the hypothesis that the observed photophysical behavior could be affected by photoswitch-wall interactions in the COF matrix. Notably, to eliminate the possibility of restricted switching caused by chelation of copper cations used as a catalyst in the CuAAC reaction, the resulted photoswitch-coordinated framework was simultaneously washed with acetonitrile and irradiated with 590-nm light to convert merocyanine to spiropyran. However, these attempts did not result in restoration of solution-like behavior of spiropyran derivatives. Taking into consideration some of the possible mechanisms of such limited photoisomerization (i.e., potential photoswitch-wall interactions), we changed the direction towards studies of MOFs with integrated photoswitchable molecules, taking advantage of 3D frameworks possessing different pore geometry (Figure 2). Prior to photophysical studies of hydrazone-containing MOFs, we explored the photophysical behavior of **H-4** in solution (3.0 mM in DMSO) using UV/Vis spectroscopy. Upon irradiation with 340-nm light, we observed a decrease in the broad absorption band centered at 330 nm followed by its increase after exposure to visible light (λ_{ex} = 405 nm, Figure S43). As shown in Figures 5 and 6, mimicking these studies in the solid-state using hydrazone-containing UiO-67 and PCN-700 resulted in similar behavior: a decrease in the absorption between 400 and 600 nm upon irradiation with 340-nm light and a subsequent increase upon exposure to visible light. As a source of visible light, we used a tungsten-halogen lamp with a 400-nm long-pass filter to cut off the UV range which could induce the reverse photoisomerization process.

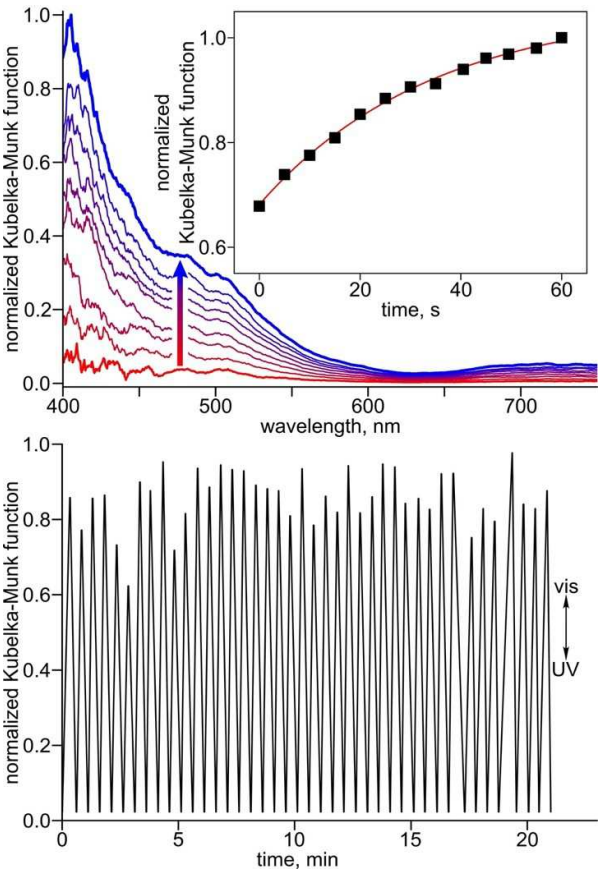

Figure 5. (*top*) Normalized diffuse reflectance spectra demonstrating isomerization from *E*-**H-4**-UiO-67 (red) to *Z*-**H-4**-UiO-67 (blue). Inset shows the kinetics data demonstrating intensity enhancement at 405 nm upon exposure to visible light. (*bottom*) Optical cycling of **H-4**-UiO-67 upon alternation with 340 nm and visible light (400–800 nm).

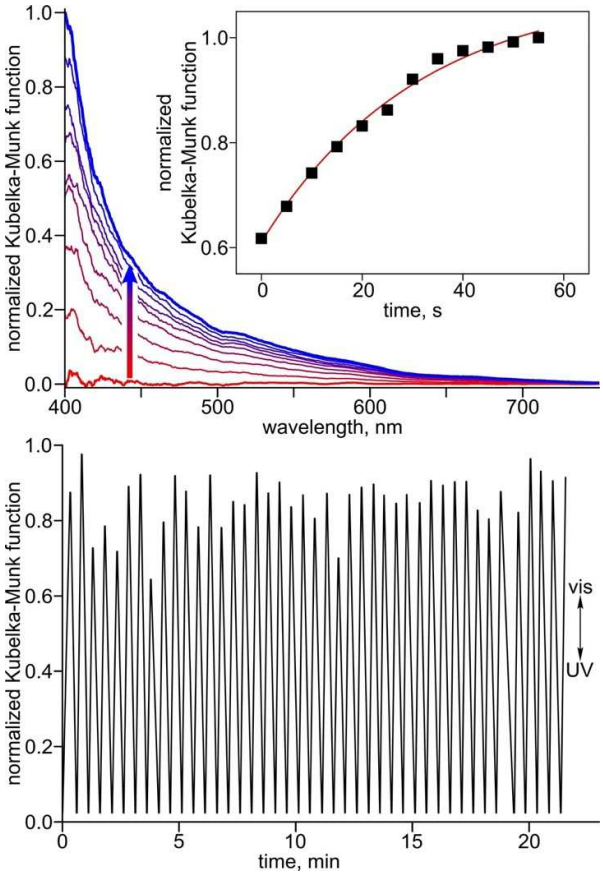

Figure 6. (*top*) Normalized diffuse reflectance spectra demonstrating isomerization from *E*-**H-4**-PCN-700 (red) to *Z*-**H-4**-PCN-700 (blue). Inset shows the kinetics data demonstrating intensity enhancement at 405 nm upon exposure to visible light. (*bottom*) Optical cycling of **H-4**-PCN-700 upon alternation with 340 nm and visible light (400–800 nm).

As a next step, we estimated the rate of isomerization for the hydrazone linker in solution and compared it with the coordinatively-immobilized one in UiO-67 and PCN-700 using a first-order model as shown in Figures 5 and 6. According to our analysis, a rate of $2.0\times10^{-2}\,s^{-1}$ ($R^2=0.991$) was estimated for *E*-to-*Z* photoisomerization of **H-4** in solution (3.0 mM in dimethyl sulfoxide (DMSO)). Remarkably, the determined photoisomerization rates for coordinatively integrated photoswitch was comparable with its behavior in solution. Thus, the estimated rates were found to be $2.9\times10^{-2}\,s^{-1}$ ($R^2=0.996$) and $3.2\times10^{-2}\,s^{-1}$ ($R^2=0.991$) for hydrazone linker integrated in UiO-67 and PCN-700, respectively, and therefore, solution-like photophysical properties of this hydrazone derivative could be promoted by a 3D MOF matrix. The observed difference in photoisomerization rate constants for UiO-67 and PCN-700 could potentially be attributed to the framework topology. For instance, the presence of unsaturated metal nodes in PCN-700 (<12 linkers per node) could contribute to the framework flexibility and promote photoisomerization.[96] Furthermore, we performed optical cycling experiments on the hydrazone-integrated Zr-MOFs by irradiating the sample with 340-nm light for 15 seconds followed by 15 seconds of measurement (i.e., exposure to visible light). As previously stated, the major absorbance features of each sample increased between 400 and 600 nm with visible light irradiation and decreased with UV light irradiation. The hydrazone-based linker exhibited up to 50 cycles upon integration into the UiO-67 and PCN-700 scaffolds (Figures 5 and 6, respectively).

As a next step, we explored the possibility to use photoswitchable behavior of hydrazone-based linkers to modulate, for instance, the FRET processes upon alternation of excitation wavelengths (Scheme 1). Selection of the suitable donor-acceptor pair was based on several criteria.[97,98] First, the emission profile of the donor must overlap with the absorbance profile of the acceptor. Second, the excitation wavelength for the donor should not directly excite the acceptor. That is, excitation of the acceptor should only occur via energy transfer from the donor. As a proof of concept, we used coordinatively-immobilized **H-4** as a donor while rhodamine 6G (R6G) dye immobilized as a guest in

the MOF pores has been selected as an appropriate acceptor. The R6G dye possesses the appropriate size of 12 Å to fit into 12×16 Å octahedral "windows" of the UiO-67 MOF. At the same time, a major absorbance feature of the dye is centered at $\lambda_{max}=528$ nm (Figure 7), which overlaps with the emission profile of coordinatively immobilized **H-4** ($\lambda_{max}=$ 470 nm, $\lambda_{ex}=300$ nm). Moreover, excitation of **H-4**-UiO-67 was possible without direct excitation of R6G, and the absorbance of **H-4**-UiO-67 did not overlap with that of R6G. Figure 7 shows the emission spectra of **H-4**-UiO-67 when stored in the dark and after exposure to 340 nm, and as anticipated, irradiation with the appropriate excitation wavelengths resulted in changes in the emission profile. Specifically, irradiation with 340 nm resulted in 1.7-fold emission enhancement, which was diminished upon exposure to the 405-nm excitation wavelength.

For integration of R6G as a guest within the framework, **H-4**-UiO-67 was soaked for 24 h in solution of R6G in DMF. The resulting polycrystalline material was collected by filtration and rinsed with DMF and ethanol. We evaluated the potential for FRET by calculating the spectral overlap function, J, using the emission profile of **H-4**-UiO-67 (donor, $F(\lambda)$) and molar extinction coefficient spectrum of R6G (acceptor, $\varepsilon(\lambda)$) in solution by the following equation: $J=\int f(\lambda)d\lambda$, $f(\lambda)=F(\lambda)\varepsilon(\lambda)\lambda^4$. As a result, J was estimated to be $1.58\times10^{-13}\,M^{-1}cm^2$. As a next step, we estimated the Förster critical radius, R_o, to be 3.55 nm using the following formula R_o (cm) $=(8.79\times10^{-25}\times\kappa^2 n^{-4}Q_d J)^{1/6}$, where Q_d is the quantum yield of **H-4** in solution (1.0 μM in toluene), κ^2 is an orientation factor approximated to 2/3, and n is a refractive index approximated to 1.[99] To evaluate FRET efficiency, we performed time-resolved fluorescence measurements of the donor in the presence, R6G@**H-4**-UiO-67, and absence of acceptor, **H-4**-UiO-67, using a 425–475-nm band-pass filter to remove any interference with R6G emission. The amplitude-weighted average lifetimes for donor in the absence (τ_D) and presence ($\tau_{D\text{-}A}$) of the acceptor were found to be $\tau_D=0.640$ ns and $\tau_{D\text{-}A}=0.407$ ns for **H-4**-UiO-67 and R6G@**H-4**-UiO-67, respectively. Thus, FRET efficiency (E) was estimated to be 36 % based on $E=(1\text{-}\tau_{D\text{-}A}/\tau_D)\times100\,\%$.[100]

As a next step, we probed the ability to tune energy transfer efficiency through modulation of the donor emission upon **H-4** photoisomerization. Based on changes in the emission profile (Figure 7) and, as a result, the spectral overlap function, we hypothesized that the corresponding FRET efficiency could be tuned upon photoisomerization. Thus, we performed similar time-resolved photoluminescence measurements for two isomers of **H-4** coordinatively immobilized into UiO-67 in the presence and absence of the R6G acceptor. The measurements for the coordinatively immobilized Z isomer are described above, and therefore, we repeated the same set of experiments for the E isomer of **H-4** integrated within UiO-67. Similar to our previous results, the lifetime of **H-4**-UiO-67 decreased in the presence of R6G, supporting the hypothesis that ET occurs within the system. The lifetimes for τ_D (*E*-**H-4**-UiO-67) and $\tau_{D\text{-}A}$ (R6G@*E*-**H-4**-UiO-67) were estimated to be 0.88 and 0.35 ns, respectively. As a result, the estimated FRET efficiency in the case of *E*-**H-4** incorporated into UiO-67

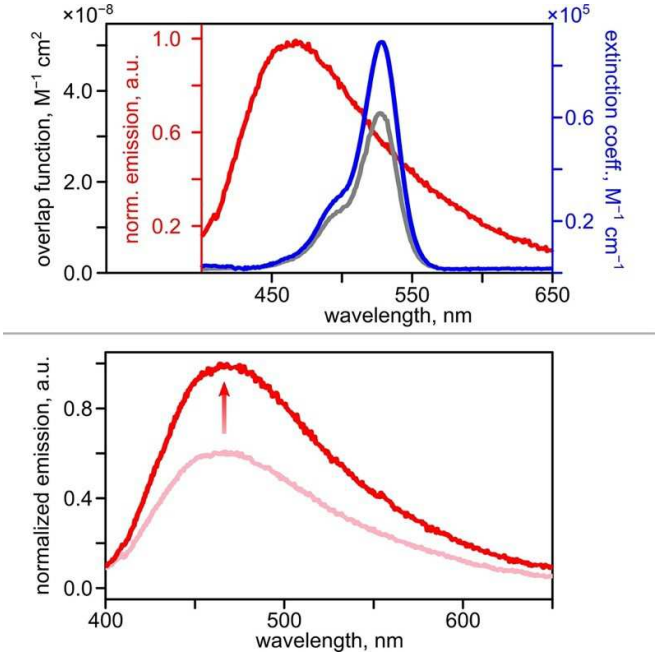

Figure 7. (*top*) Förster analysis of the ET between **H-4**-UiO-67 and R6G illustrating the spectral overlap function (gray line, left vertical axis) calculated for the measured emission spectrum of **H-4**-UiO-67 (red line, arbitrary scale), and the molar extinction spectrum of R6G in methanol (25 nM, blue line, right vertical axis). (*bottom*) Emission intensity enhancement caused by photoisomerization from *Z*-**H-4**-UiO-67 (pink) to *E*-**H-4**-UiO-67 (red) upon excitation with a 340-nm wavelength.

was found to be 60 % versus 36 % calculated for coordinatively immobilized *Z*-**H-4**. Thus, modulation of FRET efficiency could be promoted through switching between two states of hydrazone derivatives.

Conclusion

The foregoing results demonstrate for the first time that a 3D scaffold confinement environment could promote efficient photoisomerization of coordinatively-immobilized sterically-demanding hydrazone-based photoswitches. Furthermore, using three novel hydrazone derivatives, we probed the effect of porous scaffold dimensionality and showed the conceptual difference in photophysical behavior of photochromic compounds covalently-embedded into two-dimensional covalent-organic frameworks versus three-dimensional scaffolds using steady-state and time-resolved photoluminescence measurements supported by theoretical modeling. In particular, challenges which arose because of the limited photoisomerization ability of photoswitches when coordinatively integrated into a COF matrix could be resolved through immobilization of hydrazone derivatives into 3D porous scaffolds. Remarkably, photoisomerization kinetics determined for hydrazone-integrated MOFs is comparable with that in solution. Finally, we demonstrated the proof-of-concept of FRET efficiency modulation through switching between two hydrazone-based photoisomers. Thus, topological design of the confinement environment could be used as an efficient knob to modulate photophysics of hydrazone derivatives or similar photochromic molecules for which isomerization is accompanied by large structural transformations.

Acknowledgements

The authors are grateful for support from the NSF Award (DMR-2103722) and SC EPSCoR GEAR. N.B.S. also acknowledges support from the Dreyfus Teaching-Scholar Award supported by the Dreyfus Foundation and the Hans Fischer Fellowship. S.G. acknowledges partial support from the NSF Award (CHE-1955768) and GEAR-CRP 20GC03 award from SC EPSCoR. G. C. T. is supported by the National Science Foundation Graduate Research Fellowship under Grant No. DGE-2034711.

Conflict of Interest

The authors declare no conflict of interest.

Data Availability Statement

The data that support the findings of this study are available in the supplementary material of this article.

Keywords: Covalent-Organic Frameworks · FRET · Hydrazone · Metal-Organic Frameworks · Photochromism

[1] S. Krause, N. Hosono, S. Kitagawa, *Angew. Chem. Int. Ed.* **2020**, *59*, 15325–15341; *Angew. Chem.* **2020**, *132*, 15438–15456.
[2] S. Horike, S. S. Nagarkar, T. Ogawa, S. Kitagawa, *Angew. Chem. Int. Ed.* **2020**, *59*, 6652–6664; *Angew. Chem.* **2020**, *132*, 6716–6729.
[3] M. Grzelczak, L. M. Liz-Marzán, R. Klajn, *Chem. Soc. Rev.* **2019**, *48*, 1342–1361.
[4] A. W. Heard, J. M. Suárez, S. M. Goldup, *Nat. Chem. Rev.* **2022**, *6*, 182–196.
[5] A. B. Grommet, M. Feller, R. Klajn, *Nat. Nanotechnol.* **2020**, *15*, 256–271.
[6] J. D. Evans, V. Bon, I. Senkovska, H.-C. Lee, S. Kaskel, *Nat. Commun.* **2020**, *11*, 2690.
[7] M. Le, G. G. D. Han, *Acc. Mater. Res.* **2022**, *3*, 634–643.
[8] V. Bon, E. Brunner, A. Pöppl, S. Kaskel, *Adv. Funct. Mater.* **2020**, *30*, 1907847.
[9] M. A. Gerkman, G. G. D. Han, *Joule* **2020**, *4*, 1621–1625.
[10] C. Gu, N. Hosono, J.-J. Zheng, Y. Sato, S. Kusaka, S. Sakaki, S. Kitagawa, *Science* **2019**, *363*, 387–391.
[11] S. Krause, V. Bon, I. Senkovska, U. Stoeck, D. Wallacher, D. M. Többens, S. Zander, R. S. Pillai, G. Maurin, F.-X. Coudert, S. Kaskel, *Natrue* **2016**, *532*, 348–352.
[12] Q. Chen, S. Xian, X. Dong, Y. Liu, H. Wang, D. H. Olson, L. J. Williams, Y. Han, X.-H. Bu, J. Li, *Angew. Chem. Int. Ed.* **2021**, *60*, 10593–10597; *Angew. Chem.* **2021**, *133*, 10687–10691.
[13] X. Chen, H. Xie, E. R. Lorenzo, C. J. Zeman, Y. Qi, Z. H. Syed, A. E. B. S. Stone, Y. Wang, S. Goswami, P. Li, T. Islamoglu, E. A. Weiss, J. T. Hupp, G. C. Schatz, M. R. Wasielewski, O. K. Farha, *J. Am. Chem. Soc.* **2022**, *144*, 2685–2693.
[14] J. R. J. Maynard, P. Gallagher, D. Lozano, P. Butler, S. M. Goldup, *Nat. Chem.* **2022**, *14*, 1038–1044.
[15] D. Bessinger, K. Muggli, M. Beetz, F. Auras, T. Bein, *J. Am. Chem.* **2021**, *143*, 7351–7357.
[16] J. Scelle, H. Vervoitte, L. Bouteiller, L.-M. Chamoreau, M. Sollogoub, G. Vives, B. Hasenknopf, *Chem. Sci.* **2022**, *13*, 2218–2225.
[17] M. A. Gerkman, R. S. L. Gibson, J. Calbo, Y. Shi, M. J. Fuchter, G. G. D. Han, *J. Am. Chem. Soc.* **2020**, *142*, 8688–8695.
[18] S. Wannapaiboon, A. Schneemann, I. Hante, M. Tu, K. Epp, A. L. Semrau, C. Sternemann, M. Paulus, S. J. Baxter, G. Kieslich, R. A. Fischer, *Nat. Commun.* **2019**, *10*, 346.
[19] H. Wang, M. Warren, J. Jagiello, S. Jensen, S. K. Ghose, K. Tan, L. Yu, T. J. Emge, T. Thonhauser, J. Li, *J. Am. Chem. Soc.* **2020**, *142*, 20088–20097.
[20] B. Doistau, L. Benda, J.-L. Cantin, L.-M. Chamoreau, E. Ruiz, V. Marvaud, B. Hasenknopf, G. Vives, *J. Am. Chem. Soc.* **2017**, *139*, 9213–9220.
[21] B. Pattengale, S. Yang, J. Ludwig, Z. Huang, X. Zhang, J. Huang, *J. Am. Chem. Soc.* **2016**, *138*, 8072–8075.
[22] G. A. Leith, C. R. Martin, A. Mathur, P. Kittikhunnatham, K. C. Park, N. B. Shustova, *Adv. Energy Mater.* **2022**, *12*, 2100441.
[23] A. M. Rice, C. R. Martin, V. A. Galitskiy, A. A. Berseneva, G. A. Leith, N. B. Shustova, *Chem. Rev.* **2020**, *120*, 8790–8813.
[24] A. B. Grommet, L. M. Lee, R. Klajn, *Acc. Chem. Res.* **2020**, *53*, 2600–2610.
[25] A. Gonzalez, E. S. Kengmana, M. V. Fonseca, G. G. D. Han, *Mater. Today* **2020**, *6*, 100058.
[26] Y. Zheng, H. Sato, P. Wu, H. J. Jeon, R. Matsuda, S. Kitagawa, *Nat. Commun.* **2017**, *8*, 100.

[27] M. Canton, A. B. Grommet, L. Pesce, J. Gemen, S. Li, Y. Diskin-Posner, A. Credi, G. M. Pavan, J. Andréasson, R. Klajn, *J. Am. Chem. Soc.* **2020**, *142*, 14557–14565.
[28] M. Weißenfels, J. Gemen, R. Klajn, *Chem* **2021**, *7*, 23–37.
[29] S. Krause, J. D. Evans, V. Bon, S. Crespi, W. Danowski, W. R. Browne, S. Ehrling, F. Walenszus, D. Wallacher, N. Grimm, D. M. Többens, M. S. Weiss, S. Kaskel, B. L. Feringa, *Nat. Commun.* **2022**, *13*, 1951.
[30] Z. Chu, Y. Han, T. Bian, S. De, P. Král, R. Klajn, *J. Am. Chem. Soc.* **2019**, *141*, 1949–1960.
[31] G. G. D. Han, H. Li, J. C. Grossman, *Nat. Commun.* **2017**, *8*, 1446.
[32] M. A. Gerkman, J. K. Lee, X. Li, Q. Zhang, M. Windley, M. V. Fonseca, Y. Lu, J. H. Warner, G. G. D. Han, *ACS Nano* **2020**, *14*, 153–165.
[33] J. Lu, B. Pattengale, Q. Liu, S. Yang, W. Shi, S. Li, J. Huang, J. Zhang, *J. Am. Chem. Soc.* **2018**, *140*, 13719–13725.
[34] C. R. Martin, K. C. Park, G. A. Leith, J. Yu, A. Mathur, G. R. Wilson, G. B. Gange, E. L. Barth, R. T. Ly, O. M. Manley, K. L. Forrester, S. G. Karakalos, M. D. Smith, T. M. Makris, A. K. Vannucci, D. V. Peryshkov, N. B. Shustova, *J. Am. Chem. Soc.* **2022**, *144*, 4457–4468.
[35] D. Samanta, D. Galaktionova, J. Gemen, L. J. W. Shimon, Y. Diskin-Posner, L. Avram, P. Král, R. Klajn, *Nat. Commun.* **2018**, *9*, 641.
[36] M. A. Gerkman, S. Yuan, P. Duan, J. Taufan, K. Schmidt-Rohr, G. G. D. Han, *Chem. Commun.* **2019**, *55*, 5813–5816.
[37] X. Gong, J. Zhou, K. J. Hartieb, C. Miller, P. Li, O. K. Farha, J. T. Hupp, R. M. Young, M. R. Wasielewski, J. F. Stoddart, *J. Am. Chem. Soc.* **2018**, *140*, 6540–6544.
[38] T. Koshiyama, M. Shirai, T. Hikage, H. Tabe, K. Tanaka, S. Kitagawa, T. Ueno, *Angew. Chem. Int. Ed.* **2011**, *50*, 4849–4852; *Angew. Chem.* **2011**, *123*, 4951–4954.
[39] S. M. Landge, I. Aprahamian, *J. Am. Chem. Soc.* **2009**, *131*, 18269–18271.
[40] B. Shao, I. Aprahamian, *Chem* **2020**, *6*, 2162–2173.
[41] Q. Qiu, S. Yang, M. A. Gerkman, H. Fu, I. Aprahamian, G. G. D. Han, *J. Am. Chem. Soc.* **2022**, *144*, 12627–12631.
[42] R. Liang, J. Samanta, B. Shao, M. Zhang, R. J. Staples, A. D. Chen, M. Tang, Y. Wu, I. Aprahamian, C. Ke, *Angew. Chem. Int. Ed.* **2021**, *60*, 23176–23181; *Angew. Chem.* **2021**, *133*, 23360–23365.
[43] H. L. Nguyen, C. Gropp, N. Hanikel, A. Möckel, A. Lund, O. M. Yaghi, *ACS Cent. Sci.* **2022**, *8*, 926–932.
[44] S. Yang, J. D. Harris, A. Lambai, L. L. Jeliazkov, G. Mohanty, H. Zeng, A. Priimagi, I. Aprahamian, *J. Am. Chem. Soc.* **2021**, *143*, 16348–16353.
[45] S. Yang, D. Larsen, M. Pellegrini, S. Meier, D. F. Mierke, S. R. Beeren, I. Aprahamian, *Chem* **2021**, *7*, 2190–2200.
[46] B. Shao, H. Qian, Q. Li, I. Aprahamian, *J. Am. Chem. Soc.* **2019**, *141*, 8364–8371.
[47] B. Shao, M. Baroncini, H. Qian, L. Bussotti, M. D. Donato, A. Credi, I. Aprahamian, *J. Am. Chem. Soc.* **2018**, *140*, 12323–12327.
[48] G. A. Leith, C. R. Martin, J. M. Mayers, P. Kittikhunnatham, R. W. Larsen, N. B. Shustova, *Chem. Soc. Rev.* **2021**, *50*, 4382–4410.
[49] C. R. Martin, P. Kittikhunnatham, G. A. Leith, A. A. Berseneva, K. C. Park, A. B. Greytak, N. B. Shustova, *Nano Res.* **2021**, *14*, 338–354.
[50] P. K. Kundu, G. L. Olsen, V. Kiss, R. Klajn, *Nat. Commun.* **2014**, *5*, 3588.
[51] A. C. Pratt, *Chem. Soc. Rev.* **1977**, *6*, 63–81.
[52] L. A. Tatum, X. Su, I. Aprahamian, *Acc. Chem. Res.* **2014**, *47*, 2141–2149.
[53] I. Aprahamian, *Chem. Commun.* **2017**, *53*, 6674–6684.
[54] M. Jeong, J. Park, K. Lee, S. Kwon, *J. Visualization* **2022**, *180*, e63398.
[55] J. Dong, V. Wee, S. B. Peh, D. Zhao, *Angew. Chem. Int. Ed.* **2021**, *60*, 16279–16292; *Angew. Chem.* **2021**, *133*, 16415–16428.
[56] F. Castiglioni, W. Danowski, J. Perego, F. K.-C. Leung, P. Sozzani, S. Bracco, S. J. Wezenberg, A. Comotti, B. L. Feringa, *Nat. Chem.* **2020**, *12*, 595–602.
[57] H.-C. Zhou, J. R. Long, O. M. Yaghi, *Chem. Rev.* **2012**, *112*, 673–674.
[58] H. Deng, S. Grunder, K. E. Cordova, C. Valente, H. Furukawa, M. Hmadeh, F. Gándara, A. C. Whalley, Z. Liu, S. Asahina, H. Kazumori, M. O'Keeffe, O. Terasaki, J. F. Stoddart, O. M. Yaghi, *Science* **2012**, *336*, 1018–1023.
[59] J. Liu, T. A. Goetjen, Q. Wang, J. G. Knapp, M. C. Wasson, Y. Yang, Z. H. Syed, M. Delferro, J. M. Notestein, O. M. Farha, J. T. Hupp, *Chem. Soc. Rev.* **2022**, *51*, 1045–1097.
[60] R. Medishetty, J. K. Zareba, D. Mayer, M. Samoć, R. A. Fischer, *Chem. Soc. Rev.* **2017**, *46*, 4976–5004.
[61] C. R. Kim, T. Uemura, S. Kitagawa, *Chem. Soc. Rev.* **2016**, *45*, 3828–3845.
[62] M. Woellner, S. Hausdorf, N. Klein, P. Mueller, M. W. Smith, S. Kaskel, *Adv. Mater.* **2018**, *30*, 1704679.
[63] Z. Chen, K. O. Kirlikovali, P. Li, O. K. Farha, *Acc. Chem. Res.* **2022**, *55*, 579–591.
[64] Z. Ji, H. Wang, S. Canossa, S. Wuttke, O. M. Yaghi, *Adv. Funct. Mater.* **2020**, *30*, 2000238.
[65] H. Wang, W. P. Lustig, J. Li, *Chem. Soc. Rev.* **2018**, *47*, 4729–4756.
[66] W. P. Lustig, J. Li, *Coord. Chem. Rev.* **2018**, *373*, 116–147.
[67] C. S. Diercks, O. M. Yaghi, *Science* **2017**, *355*, eaal1585.
[68] N. B. Shustova, *Nat. Commun.* **2020**, *11*, 5329, https://doi.org/10.1038/s41467-020-19299-3.
[69] Z. Liu, K. Zhang, G. Huang, B. Xu, Y.-L. Hong, X. Wu, Y. Nishiyama, S. Horike, G. Zhang, S. Kitagawa, *Angew. Chem. Int. Ed.* **2022**, *61*, e202110695; *Angew. Chem.* **2022**, *134*, e202110695.
[70] I. M. Hönicke, I. Senkovska, V. Bon, I. A. Baburin, N. Bönisch, S. Raschke, J. D. Evans, S. Kaskel, *Angew. Chem. Int. Ed.* **2018**, *57*, 13780–13783; *Angew. Chem.* **2018**, *130*, 13976–13979.
[71] H. Lyu, H. Li, N. Hanikel, K. Wang, O. M. Yaghi, *J. Am. Chem. Soc.* **2022**, *144*, 12989–12995.
[72] P. M. Stanley, J. Haimerl, C. Thomas, A. Urstoeger, M. Schuster, N. B. Shustova, A. Casini, B. Rieger, J. Warnan, R. A. Fischer, *Angew. Chem. Int. Ed.* **2021**, *60*, 17854–17860; *Angew. Chem.* **2021**, *133*, 17998–18004.
[73] A. Atilgan, M. M. Cetin, J. Yu, Y. Beldjoudi, J. Liu, C. L. Stern, F. M. Cetin, T. Islamoglu, O. K. Farha, P. Deria, J. F. Stoddart, J. T. Hupp, *J. Am. Chem. Soc.* **2020**, *142*, 18554–18564.
[74] Y. Chen, F. Jiménez-Ángeles, B. Qiao, M. D. Krzyaniak, F. Sha, S. Kato, X. Gong, C. T. Buru, Z. Chen, X. Zhang, N. C. Gianneschi, M. R. Wasielewski, M. Olvera de la Cruz, O. K. Farha, *J. Am. Chem. Soc.* **2020**, *142*, 18576–18582.
[75] S. Yang, W. Hu, X. Zhang, P. He, B. Pattengale, C. Liu, M. Cendejas, I. Hermans, X. Zhang, J. Zhang, J. Huang, *J. Am. Chem. Soc.* **2018**, *140*, 14614–14618.
[76] A. M. Rice, E. A. Dolgopolova, B. J. Yarbrough, G. A. Leith, C. R. Martin, K. S. Stephenson, R. A. Heugh, A. J. Brandt, D. A. Chen, S. G. Karakalos, M. D. Smith, K. B. Hatzell, P. J. Pellechia, S. Garashchuk, N. B. Shustova, *Angew. Chem. Int. Ed.* **2018**, *57*, 11310–11315; *Angew. Chem.* **2018**, *130*, 11480–11485.
[77] G. Zhang, Y.-L. Hong, Y. Nishiyama, S. Bai, S. Kitagawa, S. Horike, *J. Am. Chem. Soc.* **2019**, *141*, 1227–1234.
[78] M. Kalaj, S. M. Cohen, *ACS Cent. Sci.* **2020**, *6*, 1046–1057.

[79] T. Islamoglu, S. Goswami, Z. Li, A. J. Howarth, O. K. Farha, J. T. Hupp, *Acc. Chem. Res.* **2017**, *50*, 805–813.
[80] L. Guo, S. Jia, C. S. Diercks, X. Yang, S. A. Alshmimri, O. M. Yaghi, *Angew. Chem. Int. Ed.* **2020**, *59*, 2023–2027; *Angew. Chem.* **2020**, *132*, 2039–2043.
[81] D. E. Williams, E. A. Dolgopolova, P. J. Pellechia, A. Palukoshka, T. J. Wilson, R. Tan, J. M. Maier, A. B. Greytak, M. D. Smith, J. A. Krause, N. B. Shustova, *J. Am. Chem. Soc.* **2015**, *137*, 2223–2226.
[82] S. Dissegna, K. Epp, W. R. Heinz, G. Kieslich, R. A. Fischer, *Adv. Mater.* **2018**, *30*, 1704501.
[83] G. A. Leith, A. M. Rice, B. J. Yarbrough, A. A. Berseneva, R. T. Ly, C. N. Buck, D. Chusov, A. J. Brandt, D. A. Chen, B. W. Lamm, M. Stefik, K. S. Stephenson, M. D. Smith, A. K. Vannucci, P. J. Pellechia, S. Garashchuk, N. B. Shustova, *Angew. Chem. Int. Ed.* **2020**, *59*, 6000–6006; *Angew. Chem.* **2020**, *132*, 6056–6062.
[84] I. Abánades Lázaro, C. J. R. Wells, R. S. Forgan, *Angew. Chem. Int. Ed.* **2020**, *59*, 5211–5217; *Angew. Chem.* **2020**, *132*, 5249–5255.
[85] H. Lyu, O. I.-F. Chen, N. Hanikel, M. I. Hossain, R. W. Flaig, X. Pei, A. Amin, M. D. Doherty, R. K. Impastato, T. G. Glover, D. R. Moore, O. M. Yaghi, *J. Am. Chem. Soc.* **2022**, *144*, 2387–2396.
[86] T. M. McDonald, J. A. Mason, X. Kong, E. D. Bloch, D. Gygi, A. Dani, V. Crocellà, F. Giordanino, S. O. Odoh, W. S. Drisdell, B. Vlaisavljevich, A. L. Dzubak, R. Poloni, S. K. Schnell, N. Planas, K. Lee, T. Pascal, L. F. Wan, D. Prendergast, J. B. Neaton, B. Smit, J. B. Kortright, L. Gagliardi, S. Bordiga, J. A. Reimer, J. R. Long, *Nature* **2015**, *519*, 303–308.
[87] Q. Chen, J. Sun, P. Li, I. Hod, P. Z. Moghadam, Z. S. Kean, R. Q. Snurr, J. T. Hupp, O. K. Farha, J. F. Stoddart, *J. Am. Chem. Soc.* **2016**, *138*, 14242–14245.
[88] F. Haase, B. V. Lotsch, *Chem. Soc. Rev.* **2020**, *49*, 8469–8500.
[89] L. Gilmanova, V. Bon, L. Shupletsov, D. Pohl, M. Rauche, E. Brunner, S. Kaskel, *J. Am. Chem. Soc.* **2021**, *143*, 18368–18373.
[90] J. B. DeCoste, G. W. Peterson, H. Jasuja, T. G. Glover, Y.-g. Huang, K. S. Walton, *J. Mater. Chem. A* **2013**, *1*, 5642–5650.
[91] S. Yuan, W. Lu, Y.-P. Chen, Q. Zhang, T.-F. Liu, D. Feng, X. Wang, J. Qin, H.-C. Zhou, *J. Am. Chem. Soc.* **2015**, *137*, 3177–3180.
[92] M. J. Katz, Z. J. Brown, Y. J. Colón, P. W. Siu, K. A. Scheidt, R. Q. Snurr, J. T. Hupp, O. K. Farha, *Chem. Commun.* **2013**, *49*, 9449–9451.
[93] L. Valenzano, B. Civalleri, S. Chavan, S. Bordiga, M. H. Nilsen, S. Jakobsen, K. P. Lillerud, C. Lamberti, *Chem. Mater.* **2011**, *23*, 1700–1718.
[94] C. R. Martin, G. A. Leith, P. Kittikhunnatham, K. C. Park, O. A. Ejegbavwo, A. Mathur, C. R. Callahan, S. L. Desmond, M. R. Kenner, F. Ahmed, S. Pandey, M. D. Smith, S. R. Phillpot, A. B. Greytak, N. B. Shustova, *Angew. Chem. Int. Ed.* **2021**, *60*, 8072–8080; *Angew. Chem.* **2021**, *133*, 8152–8160.
[95] C. Zhao, Z. Wang, X. Gong, Q. Zhang, C. Wang, Y. Shen, *Dyes Pigm.* **2017**, *140*, 460–468.
[96] B. Qian, Z. Chang, X.-H. Bu, *Top. Curr. Chem.* **2020**, *378*, 135–173.
[97] W. P. Lustig, S. Mukherjee, N. D. Rudd, A. V. Desai, J. Li, S. K. Ghosh, *Chem. Soc. Rev.* **2017**, *46*, 3242–3285.
[98] L. Wu, C. Huang, B. P. Emery, A. C. Sedgwick, S. D. Bull, X.-P. He, H. Tian, J. Yoon, J. L. Sessler, T. D. James, *Chem. Soc. Rev.* **2020**, *49*, 5110–5139.
[99] J. R. Lakowicz, *Principles of fluorescence spectroscopy*, 3rd ed., Springer, New York, **2006**.
[100] C. Chen, B. Corry, L. Huang, N. Hildebrandt, *J. Am. Chem. Soc.* **2019**, *141*, 11123–11141.
[101] Deposition number 2192210 contains the supplementary crystallographic data for this paper. These data are provided free of charge by the joint Cambridge Crystallographic Data Centre and Fachinformationszentrum Karlsruhe Access Structures service.

Manuscript received: August 10, 2022
Accepted manuscript online: November 8, 2022
Version of record online: December 2, 2022